Available online at www.sciencedirect.com
SCIENCE DIRECT®
Composite Structures 63 (2004) 271–281
COMPOSITE STRUCTURES
www.elsevier.com/locate/compstruct

Nonlinear finite element analysis of reinforced concrete beams strengthened by fiber-reinforced plastics

Hsuan-Teh Hu *, Fu-Ming Lin, Yih-Yuan Jan

Department of Civil Engineering, National Cheng Kung University, Tainan 701, Taiwan

Abstract

Numerical analyses are performed using the ABAQUS finite element program to predict the ultimate loading capacity of rectangular reinforced concrete beams strengthened by fiber-reinforced plastics applied at the bottom or on both sides of these beams. Nonlinear material behavior, as it relates to steel reinforcing bars, plain concrete, and fiber-reinforced plastics is simulated using appropriate constitutive models. The influences of fiber orientation, beam length and reinforcement ratios on the ultimate strength of the beams are investigated. It has been shown that the use of fiber-reinforced plastics can significantly increase the stiffnesses as well as the ultimate strengths of reinforced concrete beams. In addition, with the same fiber-reinforced plastics layer numbers, the ultimate strengths of beams strengthened by fiber-reinforced plastics at the bottom of the beams are much higher than those strengthened by fiber-reinforced plastics on both sides of the beams.

Keywords: Reinforced concrete beams; Strengthened; Fiber-reinforced plastics

1. Introduction

The traditional material used in the strengthening of concrete structures is steel. Because of its drawbacks of low corrosion resistance and of handling problems involving excessive size and weight, there is a need for the engineering community to look for alternatives. Due to lightweight, high strength and good fatigue and corrosion properties, fiber-reinforced plastics (FRP) have been intensively used in the repair and strengthening of aerospace structures [1–4]. Though the study of using FRP to strengthen reinforced concrete structures just started in the 1990s [5–15], the technology is currently widely used.

To study the behavior of reinforced concrete structures strengthened by FRP, the fundamental step is to understand the nonlinear behavior of the constitutive materials, reinforced concrete and FRP, separately. The nonlinear behavior of reinforced concrete such as concrete cracking, tension stiffening, shear retention, concrete plasticity and yielding of reinforcing steel have been extensively studied by various researchers and numerous proper constitutive laws have been proposed [16–21]. However, in the literature, most studies of reinforced concrete structures strengthened by FRP have assumed that the behavior of FRP is linear. It is well known that unidirectional fibrous composites exhibit severe nonlinearity in their in-plane shear stress–strain relations [22]. In addition, deviation from linearity is also observed with in-plane transverse loading but the degree of nonlinearity is not comparable to that observed with the in-plane shear [22,23]. Therefore, appropriate modeling of the nonlinear behavior of FRP becomes crucial.

In this investigation, proper constitutive models are introduced to simulate the nonlinear behavior of reinforced concrete and FRP. Then the finite element program ABAQUS [24] is used to perform a failure analysis of rectangular reinforced concrete beams strengthened by FRP. In the numerical analyses, two types of beams, i.e. a short beam and a long beam, and two types of reinforcement ratios, i.e. a low and a high steel percentage ratio, are considered. The aim of this research is to study the influence of beam length, reinforcement ratio and fiber orientation on the globally nonlinear behavior of rectangular reinforced concrete beams subjected to uniformly distributed load and strengthened by FRP. In addition, the improvement in stiffness and

* Corresponding author. Tel.: +886-6-2757575x63168; fax: +886-6-2358542.
E-mail address: hthu@mail.ncku.edu.tw (H.-T. Hu).

0263-8223/$ - see front matter © 2003 Elsevier Ltd. All rights reserved.
doi:10.1016/S0263-8223(03)00174-0

strength as well as the alteration of the failure mechanism of the reinforced concrete beams due to FRP are investigated.

2. Material properties and constitutive models

The materials used in the analysis involve steel reinforcing bars, concrete and FRP. Reliable constitutive models applicable to steel reinforcing bars and concrete are available in the ABAQUS material library. Thus, their input material properties and associated constitutive models are only briefly discussed. The ABAQUS program does not have a nonlinear material library for FRP. Hence, its nonlinear constitutive model is discussed here in detail. The resulting nonlinear constitutive equations for the FRP are coded in FORTRAN language as a subroutine and linked to the ABAQUS program.

2.1. Steel reinforcing bar

The steel reinforcement used in the beam is assumed to have the yielding stress

$$\sigma_y = 344.7 \text{ MPa } (50 \text{ ksi}) \tag{1}$$

while its elastic modulus is assumed to be

$$E_s = 199.9 \text{ GPa } (29000 \text{ ksi}) \tag{2}$$

The stress–strain curve of the reinforcing bar is assumed to be elastic perfectly plastic as shown in Fig. 1. In ABAQUS, the steel reinforcement is treated as an equivalent uniaxial material smeared through out the element section and the bond–slip effect between concrete and steel is not considered. In order to properly model the constitutive behavior of the reinforcement, the cross sectional area, spacing, position and orientation of each layer of steel bar within each element needs to be specified.

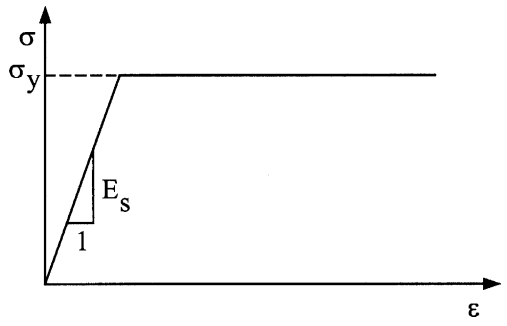

Fig. 1. Elastic perfectly plastic model for steel reinforcing bar.

2.2. Concrete

The concrete has an uniaxial compressive strength f'_c selected as

$$f'_c = 34.47 \text{ MPa } (5 \text{ ksi}) \tag{3}$$

Under uniaxial compression, the concrete strain ε_o corresponding to the peak stress f'_c is usually around the range of 0.002–0.003. A representative value suggested by ACI Committee 318 [25] and used in the analysis is

$$\varepsilon_o = 0.003 \tag{4}$$

The Poisson's ratio v_c of concrete under uniaxial compressive stress ranges from about 0.15–0.22, with a representative value of 0.19 or 0.20 [16]. In this study, the Poisson's ratio of concrete is assumed to be

$$v_c = 0.2 \tag{5}$$

The uniaxial tensile strength f'_t of concrete is difficult to measure. For this study the value is taken as [16]

$$f'_t = 0.33\sqrt{f'_c} \text{ MPa} \tag{6}$$

The initial modulus of elasticity of concrete E_c is highly correlated to its compressive strength and can be calculated with reasonable accuracy from the empirical equation [25]

$$E_c = 4700\sqrt{f'_c} \text{ MPa} \tag{7}$$

Under multiaxial combinations of loading, the failure strengths of concrete are different from those observed under uniaxial condition. However, the maximum strength envelope under multiple stress conditions seems to be largely independent of load path [26]. In ABAQUS, a Mohr–Coulomb type compression surface together with a crack detection surface is used to model the failure surface of concrete (Fig. 2). When the principal stress components of concrete are predominantly compressive, the response of the concrete is modeled by

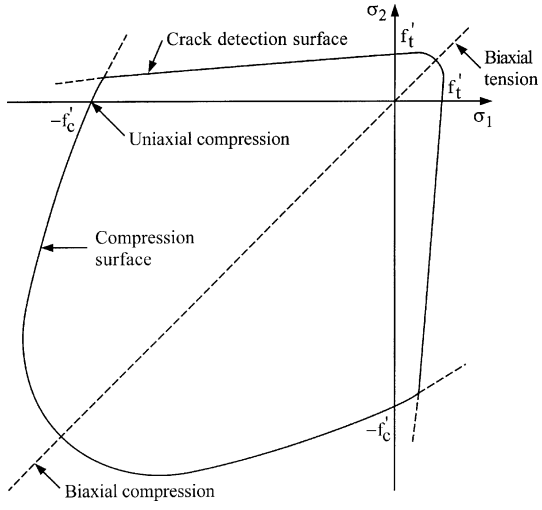

Fig. 2. Concrete failure surface in plane stress.

an elastic–plastic theory with an associated flow and an isotropic hardening rule. In tension, once cracking is defined to occur (by the crack detection surface), the orientation of the crack is stored. Damaged elasticity is then used to model the existing crack [24].

When plastic deformation occurs, there should be a certain parameter to guide the expansion of the yield surface. A commonly used approach is to relate the multidimensional stress and strain conditions to a pair of quantities, namely, the effective stress σ_c and effective strain ε_c, such that results obtained following different loading paths can all be correlated by means of the equivalent uniaxial stress–strain curve. The stress–strain relationship proposed by Saenz [27] has been widely adopted as the uniaxial stress–strain curve for concrete and it has the following form:

$$\sigma_c = \frac{E_c \varepsilon_c}{1 + (R + R_E - 2)\left(\frac{\varepsilon_c}{\varepsilon_o}\right) - (2R - 1)\left(\frac{\varepsilon_c}{\varepsilon_o}\right)^2 + R\left(\frac{\varepsilon_c}{\varepsilon_o}\right)^3} \tag{8}$$

where

$$R = \frac{R_E(R_\sigma - 1)}{(R_\varepsilon - 1)^2} - \frac{1}{R_\varepsilon}, \quad R_E = \frac{E_c}{E_o}, \quad E_o = \frac{f'_c}{\varepsilon_o}$$

and $R_\sigma = 4$, $R_\varepsilon = 4$ may be used [20]. In the analysis, Eq. (8) is taken as the equivalent uniaxial stress–strain curve for concrete and approximated by several piecewise linear segments as shown in Fig. 3.

When cracking of concrete takes place, a smeared model is used to represent the discontinuous macrocrack behavior. It is known that the cracked concrete of a reinforced concrete element can still carry some tensile stress in the direction normal to the crack, which is termed tension stiffening [16]. In this study, a simple descending line is used to model this tension stiffening phenomenon (Fig. 4). The default value of the strain ε^* at which the tension stiffening stress reduced to zero is [24]

$$\varepsilon^* = 0.001 \tag{9}$$

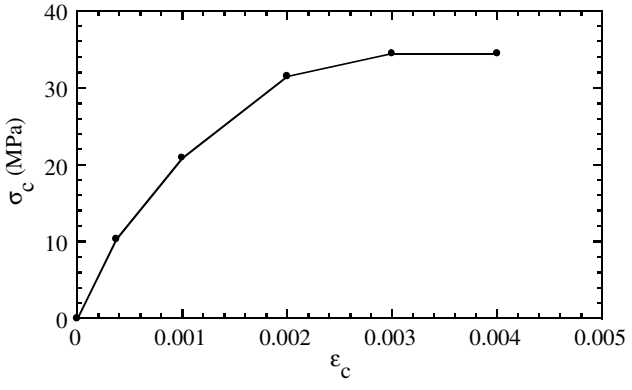

Fig. 3. Equivalent uniaxial stress–strain curve for concrete.

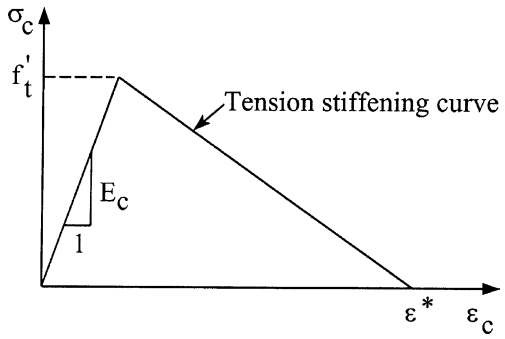

Fig. 4. Tension stiffening model.

During the postcracking stage, the cracked reinforced concrete can still transfer shear forces through aggregate interlock or shear friction, which is termed shear retention. Assuming that the shear modulus of intact concrete is G_c, then the reduced shear modulus $\widehat{G}$ of cracked concrete can be expressed as

$$\widehat{G} = \mu G_c \tag{10}$$

$$\mu = (1 - \varepsilon/\varepsilon_{max}) \tag{11}$$

where ε is the strain normal to the crack direction and ε_{max} is the strain at which the parameter μ reduces to zero (Fig. 5). Numerous analytical results have demonstrated that the particular value chosen for μ (between 0 and 1) does not appear to be critical but values greater than zero are necessary to prevent numerical instabilities [16,21]. In ABAQUS, ε_{max} is usually assumed to be a very large value, i.e., $\mu = 1$ (full shear retention). In this investigation, the default values for tension stiffening parameter $\varepsilon^* = 0.001$ and for shear retention parameter $\mu = 1$ are used.

2.3. Fiber-reinforced plastics

For fiber-reinforced plastics (Fig. 6), each lamina can be considered as an orthotropic layer in a plane stress condition. It is well known that unidirectional fibrous composites exhibit severe nonlinearity in their in-plane shear stress–strain relation. In addition, deviation from linearity is also observed with in-plane transverse loading but the degree of nonlinearity is not comparable to

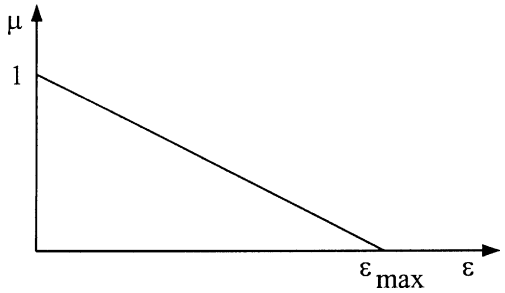

Fig. 5. Shear retention parameter.

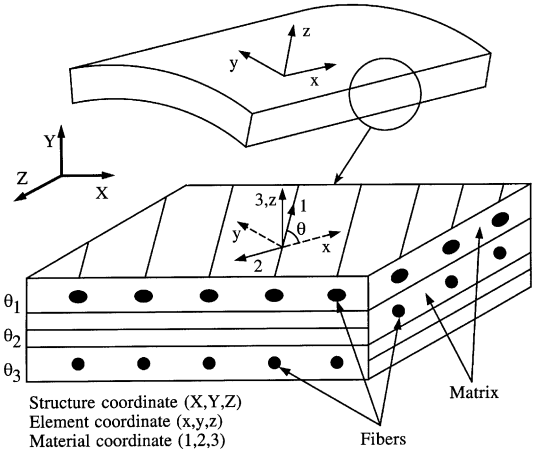

Fig. 6. Material, element and structure coordinates of fiber reinforced plastics.

that in the in-plane shear [22]. Usually, this nonlinearity associated with the transverse loading can be ignored [23]. To model the nonlinear in-plane shear behavior, the nonlinear strain–stress relation for a composite lamina suggested by Hahn and Tsai [22] is adopted. Values are given as follows:

$$\begin{Bmatrix} \varepsilon_1 \\ \varepsilon_2 \\ \gamma_{12} \end{Bmatrix} = \begin{bmatrix} \frac{1}{E_{11}} & -\frac{\nu_{21}}{E_{22}} & 0 \\ -\frac{\nu_{12}}{E_{11}} & \frac{1}{E_{22}} & 0 \\ 0 & 0 & \frac{1}{G_{12}} \end{bmatrix} \begin{Bmatrix} \sigma_1 \\ \sigma_2 \\ \tau_{12} \end{Bmatrix} + S_{6666}\tau_{12}^2 \begin{Bmatrix} 0 \\ 0 \\ \tau_{12} \end{Bmatrix} \tag{12}$$

In this model only one constant S_{6666} is required to account for the in-plane shear nonlinearity. The value of S_{6666} can be determined by a curve fit to various off-axis tension test data [22]. Let us define $\Delta\{\sigma'\} = \Delta\{\sigma_1, \sigma_2, \tau_{12}\}^{\mathrm{T}}$ and $\Delta\{\varepsilon'\} = \Delta\{\varepsilon_1, \varepsilon_2, \gamma_{12}\}^{\mathrm{T}}$. Inverting and differentiating Eq. (12), the incremental stress–strain relations are established

$$\Delta\{\sigma'\} = [Q_1']\Delta\{\varepsilon'\} \tag{13}$$

$$[Q_1'] = \begin{bmatrix} \frac{E_{11}}{1-\nu_{12}\nu_{21}} & \frac{\nu_{12}E_{22}}{1-\nu_{12}\nu_{21}} & 0 \\ \frac{\nu_{21}E_{11}}{1-\nu_{12}\nu_{21}} & \frac{E_{22}}{1-\nu_{12}\nu_{21}} & 0 \\ 0 & 0 & \frac{1}{1/G_{12}+3S_{6666}\tau_{12}^2} \end{bmatrix} \tag{14}$$

Furthermore, it is assumed that the transverse shear stresses always behave linearly and do not affect the nonlinear behavior of any in-plane shear. If we define $\Delta\{\tau_t'\} = \Delta\{\tau_{13}, \tau_{23}\}^{\mathrm{T}}$ and $\Delta\{\gamma_t'\} = \Delta\{\gamma_{13}, \gamma_{23}\}^{\mathrm{T}}$, the constitutive equations for transverse shear stresses become

$$\Delta\{\tau_t'\} = [Q_2']\Delta\{\gamma_t'\} \tag{15}$$

$$[Q_2'] = \begin{bmatrix} \alpha_1 G_{13} & 0 \\ 0 & \alpha_2 G_{23} \end{bmatrix} \tag{16}$$

where α_1 and α_2 are the shear correction factors and are taken to be 0.83 in this study.

Among existing failure criteria, the Tsai–Wu criterion [28] has been extensively used in the literature and is adopted in this analysis. Under plane stress conditions, this failure criterion has the following form:

$$F_1\sigma_1 + F_2\sigma_2 + F_{11}\sigma_1^2 + 2F_{12}\sigma_1\sigma_2 + F_{22}\sigma_2^2 + F_{66}\tau_{12}^2 = 1 \tag{17}$$

with

$$F_1 = \frac{1}{\overline{X}} + \frac{1}{\overline{X}'}, \quad F_2 = \frac{1}{\overline{Y}} + \frac{1}{\overline{Y}'}, \quad F_{11} = \frac{-1}{\overline{X}\overline{X}'}, \quad F_{22} = \frac{-1}{\overline{Y}\overline{Y}'}, \quad F_{66} = \frac{1}{\overline{S}^2}$$

The $\overline{X}$, $\overline{Y}$ and $\overline{X}'$, $\overline{Y}'$ are the lamina longitudinal and transverse strengths in tension and compression, respectively, and $\overline{S}$ is the shear strength of the lamina. Though the stress interaction term F_{12} in Eq. (17) is difficult to be determined, it has been suggested that F_{12} can be set equal to zero for practical engineering applications [29]. Therefore, $F_{12} = 0$ is used in this investigation.

During the numerical calculation, incremental loading is applied to composite plates until failures in one or more of individual plies are indicated according to Eq. (17). Since the Tsai–Wu criterion does not distinguish failure modes, the following two rules are used to determine whether the ply failure is caused by resin fracture or fiber breakage [30]:

(1) If a ply fails but the stress in the fiber direction remains less than the uniaxial strength of the lamina in the fiber direction, i.e. $\overline{X}' < \sigma_1 < \overline{X}$, the ply failure is assumed to be resin induced. Consequently, the laminate loses its capability to support transverse and shear stresses, but remains to carry longitudinal stress. In this case, the constitutive matrix of the lamina becomes

$$[Q_1'] = \begin{bmatrix} E_{11} & 0 & 0 \\ 0 & 0 & 0 \\ 0 & 0 & 0 \end{bmatrix} \tag{18}$$

(2) If a ply fails with σ_1 exceeding the uniaxial strength of the lamina, the ply failure is caused by the fiber breakage and a total ply rupture is assumed. In this case, the constitutive matrix of the lamina becomes

$$[Q_1'] = \begin{bmatrix} 0 & 0 & 0 \\ 0 & 0 & 0 \\ 0 & 0 & 0 \end{bmatrix} \tag{19}$$

The material properties for FRP used in the analysis are $E_{11} = 138$ GPa, $E_{22} = 14.5$ GPa, $G_{12} = G_{13} = 5.86$ GPa, $G_{23} = 3.52$ GPa, $S_{6666} = 7.32$ (GPa)$^{-3}$, $\overline{X} = 1450$ MPa, $\overline{X}' = -1450$ MPa, $\overline{Y} = 52$ MPa, $\overline{Y}' = -206$ MPa, $\overline{S} = 93$ MPa, $\nu_{12} = 0.21$.

During a finite element analysis, the constitutive matrix of composite materials at the integration points of shell elements must be calculated before the stiffness matrices are assembled from the element level to the structural level. For composite materials, the incremental constitutive equations of a lamina in the element coordinates (x, y, z) can be written as

$$\Delta\{\sigma\} = [Q_1]\Delta\{\varepsilon\} \tag{20}$$

$$\Delta\{\tau_t\} = [Q_2]\Delta\{\gamma_t\} \tag{21}$$

where $\Delta\{\sigma\} = \Delta\{\sigma_x, \sigma_y, \tau_{xy}\}^{\mathrm{T}}$, $\Delta\{\tau_t\} = \Delta\{\tau_{xz}, \tau_{yz}\}^{\mathrm{T}}$, $\Delta\{\varepsilon\} = \Delta\{\varepsilon_x, \varepsilon_y, \gamma_{xy}\}^{\mathrm{T}}$, $\Delta\{\gamma_t\} = \Delta\{\gamma_{xz}, \gamma_{yz}\}^{\mathrm{T}}$, and

$$[Q_1] = [T_1]^{\mathrm{T}}[Q_1'][T_1] \tag{22}$$

$$[Q_2] = [T_2]^{\mathrm{T}}[Q_2'][T_2] \tag{23}$$

$$[T_1] = \begin{bmatrix} \cos^2\theta & \sin^2\theta & \sin\theta\cos\theta \\ \sin^2\theta & \cos^2\theta & -\sin\theta\cos\theta \\ -2\sin\theta\cos\theta & 2\sin\theta\cos\theta & \cos^2\theta - \sin^2\theta \end{bmatrix} \tag{24}$$

$$[T_2] = \begin{bmatrix} \cos\theta & \sin\theta \\ -\sin\theta & \cos\theta \end{bmatrix} \tag{25}$$

The θ is measured counterclockwise from the element local x-axis to the material 1-axis (Fig. 6). Assume $\Delta\{\varepsilon_o\} = D\{\varepsilon_{xo}, \varepsilon_{yo}, \gamma_{xyo}\}^{\mathrm{T}}$ are the incremental in-plane strains at the midsurface of the shell section and $\Delta\{\kappa\} = \Delta\{\kappa_x, \kappa_y, \kappa_{xy}\}^{\mathrm{T}}$ are its incremental curvatures. The incremental in-plane strains at a distance z from the midsurface of the shell section become

$$\Delta\{\varepsilon\} = \Delta\{\varepsilon_o\} + z\Delta\{\kappa\} \tag{26}$$

Let h be the total thickness of the composite shell section, the incremental stress resultants, $\Delta\{N\} = \Delta\{N_x, N_y, N_{xy}\}^{\mathrm{T}}$, $\Delta M = \Delta\{M_x, M_y, M_{xy}\}^{\mathrm{T}}$ and $\Delta\{V\} = \Delta\{V_x, V_y\}$, can be defined as

$$\begin{Bmatrix} \Delta\{N\} \\ \Delta\{M\} \\ \Delta\{V\} \end{Bmatrix} = \int_{-h/2}^{h/2} \begin{Bmatrix} \Delta\{\sigma\} \\ z\Delta\{\sigma\} \\ \Delta\{\tau_t\} \end{Bmatrix} \mathrm{d}z \tag{27}$$

Substituting Eqs. (20), (21) and (26) into the above expression, one can obtain the stiffness matrix for the fiber composite laminate shell at the integration point as

$$\begin{Bmatrix} \Delta\{N\} \\ \Delta\{M\} \\ \Delta\{V\} \end{Bmatrix} = \int_{-h/2}^{h/2} \begin{bmatrix} [Q_1] & z[Q_1] & [0] \\ z[Q_1] & z^2[Q_1] & [0] \\ [0]^{\mathrm{T}} & [0]^{\mathrm{T}} & [Q_2] \end{bmatrix} \begin{Bmatrix} \Delta\{\varepsilon_o\} \\ \Delta\{\kappa\} \\ \Delta\{\gamma_t\} \end{Bmatrix} \mathrm{d}z \tag{28}$$

where [0] is a 3×2 null matrix.

3. Verification of the proposed material constitutive models

The validity of the material models for steel, concrete and FRP has been verified individually by testing against experimental data [24,31] and is not duplicated here. The validity of the these material models to simulate the composite behavior of reinforced concrete beam strengthened by FRP is examined in this section by comparing with the result of beam experiment performed by Shahawy et al. [10]. The dimensions of the test beam are given in Fig. 7. The beam is subjected to four-point static load up to failure. The flexural reinforcement is composed of two 13 mm diameter steel bars in tension zone and two 3 mm diameter steel bars in compression zone. The yielding strength and the elastic modulus of the reinforcing steel are $\sigma_y = 468.8$ MPa and $E_s = 199.9$ GPa. The compressive strength and the Poisson's ratio of concrete are $f_c' = 41.37$ MPa and $v_c = 0.2$. Three FRP layers with their fiber directions oriented in the axial direction of the beam are adhered to the bottom face of the beam. Each FRP layer is 0.1702 mm in thickness with tensile strength $\overline{X} = 2758$ MPa and modulus $E_{11} = 141.3$ GPa. To take the Tsai–Wu criterion into account, the following parameters are assumed: $\overline{X}' = -2758$ MPa, $\overline{Y} = 52$ MPa, $\overline{Y}' = -206$ MPa, $\overline{S} = 93$ MPa, $E_{22} = 14.5$ GPa, $G_{12} = G_{13} = 5.86$ GPa, $G_{23} = 3.52$ GPa, $S_{6666} = 7.32$ (GPa)$^{-3}$, $v_{12} = 0.21$. Since the FRP layers are subjected to uniaxial tension in fiber direction only, these assumed parameters would not affect the uniaxial tensile behavior of the FRP.

The beam has two planes of symmetry. One plane of symmetry is the x–y plane cutting beam in half longitudinally. The other plane of symmetry is the y–z plane cutting beam in half transversely. Due to symmetry, only 1/4 portion of the beam is analyzed and symmetric boundary conditions are placed along the two symmetric planes. In the finite element analysis, 8-node solid elements (three degrees of freedom per node) are used to model the reinforced concrete beams. The 1/4 beam mesh has 78 solid elements in total (26 rows in x-direction, 3 rows in y-direction and 1 row in z-direction). Because the fiber-reinforced plastics are relatively thin compared to the concrete beam, they are modeled by the

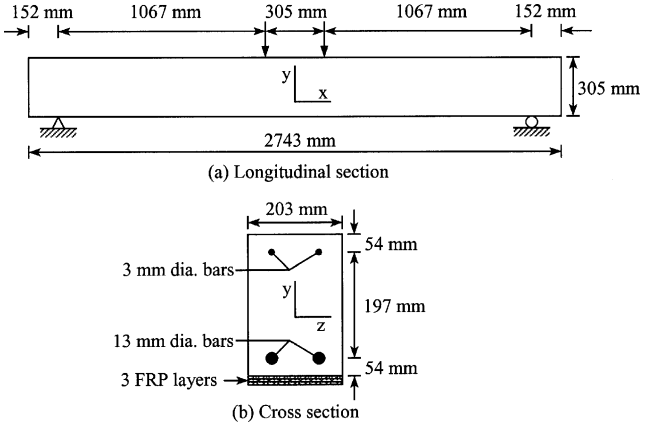

Fig. 7. Details of test beam.

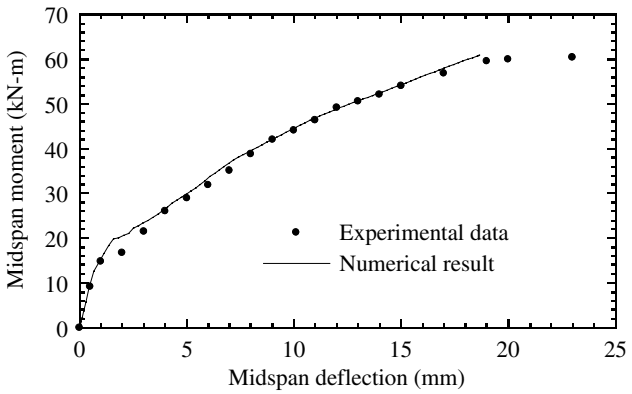

Fig. 8. Comparison of numerical and experimental results.

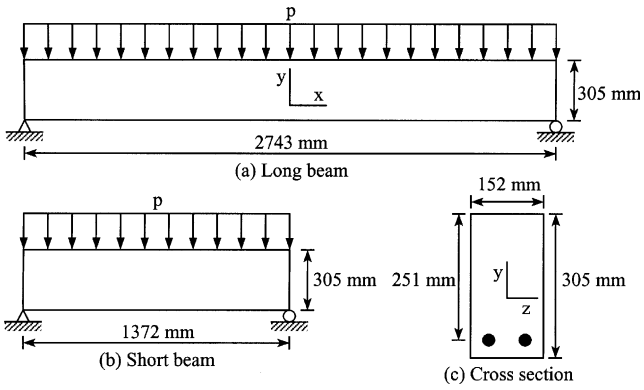

Fig. 9. Details of beams in numerical analysis.

4-node shell elements (six degrees of freedom per node). The FRP shell elements are attached to the bottom surface of the concrete beam directly and perfect bonding between FRP and the concrete is assumed.

Fig. 8 shows the moment versus deflection curves of the beam at the midspan. It can be observed that the correlation is quite good between the numerical result and the experimental data. The predicted ultimate moment 60.9 kN m is in good agreement with the experimental ultimate moment 60.4 kN m. The error is only about 0.8%. Hence, the proposed material constitutive models are proved to be able to simulate the composite behavior of reinforced concrete beam strengthened by FRP correctly.

4. Numerical analysis

4.1. Beam geometry and finite element model

In the numerical analyses, simply supported reinforced concrete beams with two types of lengths, i.e., short beam and long beam, are considered (Fig. 9). While the deflection of the long beam is primary caused by bending, the deflection of the short beam is due to both bending and shear [32]. To study the influence of reinforcement ratio, two types of reinforcement ratios, i.e. low reinforcement ratio and high reinforcement ratio, are considered. Two #4 steel bars ($\rho = 0.0066$) are used for beams with low reinforcement ratio and two #8 steel bars ($\rho = 0.0264$) are used for beams with high reinforcement ratio. Both high and low reinforcement ratios satisfy the requirement of ACI code [25], i.e. $1.4/\sigma_y \leqslant \rho \leqslant 0.75\rho_b$, where $\rho_b = 0.108$ is the reinforcement ratio for the balanced strain condition. These beams are subjected to a uniformly distributed load p (force per unit area) at the top surface of the beam and the weights of the beams are neglected. The material properties for steel, concrete and FRP discussed in Section 2 are used in the numerical analyses.

These beams again have two planes of symmetry. Therefore, only 1/4 portion of each beam is analyzed and symmetric boundary conditions are placed along the two symmetric planes. In the finite element analysis, 27-node solid elements (three degrees of freedom per node) are used to model the reinforced concrete beams. Based on the results of convergent studies [32], it was decided to use 72 elements (18 rows in x-direction, 4 rows in y-direction and 1 row in z-direction) for long beams and 36 elements (9 rows in x-direction, 4 rows in y-direction and 1 row in z-direction) for short beams. The FRP are modeled by the 8-node shell elements (six degrees of freedom per node) and attached to the outer surface of the concrete beams directly.

4.2. Ultimate analysis of reinforced concrete beams without strengthening FRP

In order to provide a base to make a comparison or show how the FRP changes the beam, ultimate analyses of ordinary reinforced concrete beams without any FRP are carried out. Fig. 10 shows the uniformly distributed load p versus the midspan deflection of the beams. The first character L or S in the figure represents long beam or short beam, respectively. The following numbers 4 or 8 stand for beams with #4 or #8 steel bars. From the figure one can observe that the stiffness and the ultimate load of the long beams (L4 and L8) are much lower than those of the short beams (S4 and S8). This is because the long beams are weaker in bending than the short beams. Generally, the reinforcement ratio does not influence the ultimate load of beams significantly. For example, the ultimate load p_u of L8 beam (71.02 kPa) is higher than that of L4 beam (68.53 kPa) by 3.63% and the ultimate load of S8 beam (151.68 kPa) is higher than that of S4 beam (146.17 kPa) by 3.77%. For the long beams, the beam with low reinforcement ratio (L4) has more ductile behavior near the ultimate loading stage than that with high reinforcement ratio (L8). However, for the short beams, the reinforcement ratio does not influence their

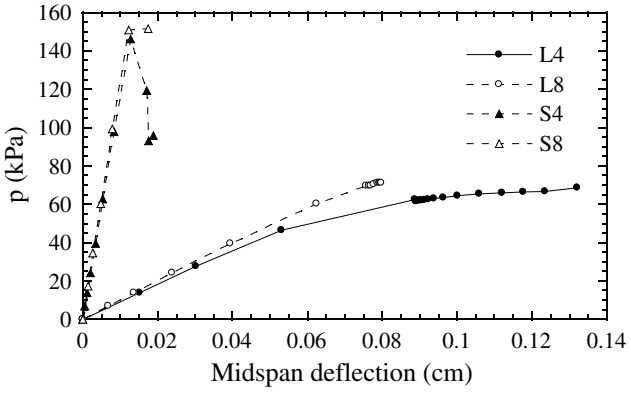

Fig. 10. Load–deflection curves of reinforced concrete beams without strengthening FRP.

behaviors prior to the ultimate loading stage significantly.

Fig. 11 shows the crack patterns of all four types of beams under ultimate loads. The black dots in the figure indicate that the integration points of the concrete elements have cracks. It can be seen that the long beams fail by bending and numerous cracks take place in the bottom of the central region of the beams. In addition, the beam with low reinforcement ratio (L4) would have more cracks than that with high reinforcement ratio (L8). The short beams fail by shear and cracks take place near the bottom of the support area. Unlike the long beams, the crack patterns for S4 and S8 beams are very similar. Hence, it can be confirmed again that the reinforcement ratio does not influence the behaviors of short beams prior to the ultimate loading stage significantly.

4.3. Ultimate analysis of reinforced concrete beams strengthened by FRP at the bottom

To increase the bending resistance of the reinforced concrete beams, we consider attaching the FRP to the bottom of the beams in this section. The thickness of each FRP layer is 1 mm (0.04 in) and the laminate lay-ups are $[0]_n$, where $n = 1, 2, 3, 4$. The fiber angle of the lamina is measured counterclockwise (through outward normal direction) from the longitudinal direction of the beams. The reason that all the fibers are placed in the axial direction of beam is because FRP has the highest stiffness and strength in its fiber direction.

Figs. 12 and 13 show the uniformly distributed load p versus the midspan deflection of reinforced concrete beams strengthened by FRP. Generally, the stiffnesses of the beams increase when the numbers of FRP layers are

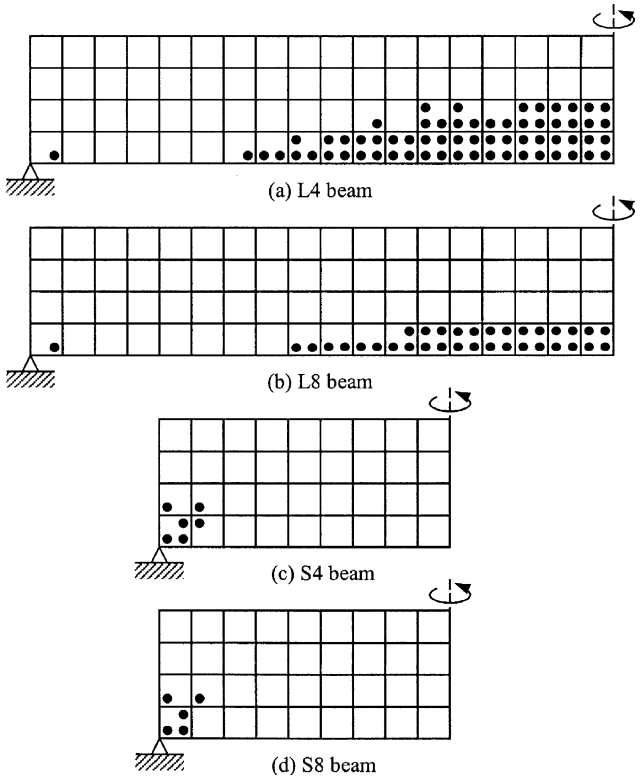

Fig. 11. Crack patterns of reinforced concrete beams without strengthening FRP and under ultimate loads.

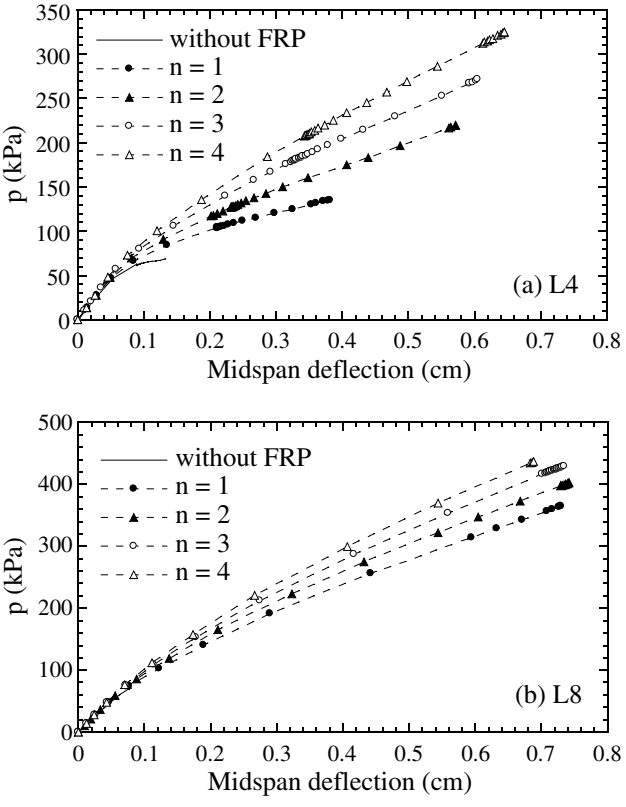

Fig. 12. Load–deflection curves of long reinforced concrete beams strengthened by $[0]_n$ FRP at the bottom.

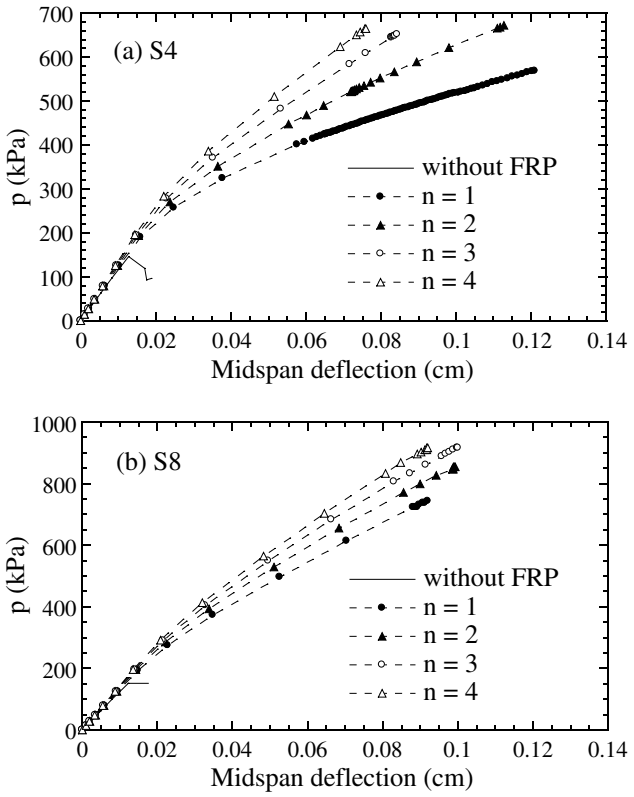

Fig. 13. Load–deflection curves of short reinforced concrete beams strengthened by $[0]_n$ FRP at the bottom.

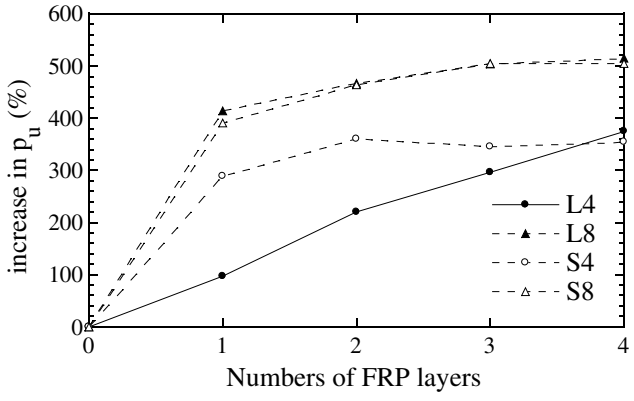

Fig. 14. Increase of p_u versus numbers of FRP layers for reinforced concrete beams strengthened by $[0]_n$ FRP at the bottom.

increased. Fig. 14 shows the increasing of the ultimate load p_u versus the numbers of FRP layers at the bottom of beams. For the long beams with low reinforcement ratio (L4), p_u seems to increase linearly with the number of FRP layers (for $n < 4$). For the other three types of beams, L8, S4 and S8, the use of one FRP layer would have the most significant effect in increasing the p_u. When the numbers of FRP layers are increased, this increase in p_u seems to approach constant values (say 500% for L8 and S8 beams; 350% for S4 beams) and becomes less significant than for the first FRP layer. It can be seen that the curves of L8 and S8 in Fig. 14 are almost identical and that the trends of the load–deflection curves in Figs. 12(b) and 13(b) are similar. This may indicate that the behaviors of the beams with high reinforcement ratio and strengthened with FRP are not influenced by the length of beam significantly. However, for beams with low reinforcement ratio and strengthened with FRP, the beam lengths do affect their behaviors significantly, as shown by Figs. 12(a), 13(a) and 14.

Fig. 15 shows the crack patterns of reinforced concrete beams strengthened by $[0]_4$ FRP at the bottom and under ultimate loads. Comparing Fig. 15 with Fig. 11, one could see that after FRP is employed at the bottom of the beams, these beams are failed in a combination of bending and shear modes, i.e., severe cracks occur at the bottom of the beam from the central region through out the support area. Generally, the beams with high reinforcement ratios and strengthened with FRP would have more cracks at the central region than those with low reinforcement ratios. On the other hand, the beams with low reinforcement ratios and strengthened with FRP would have more cracks at the support area than those with high reinforcement ratios.

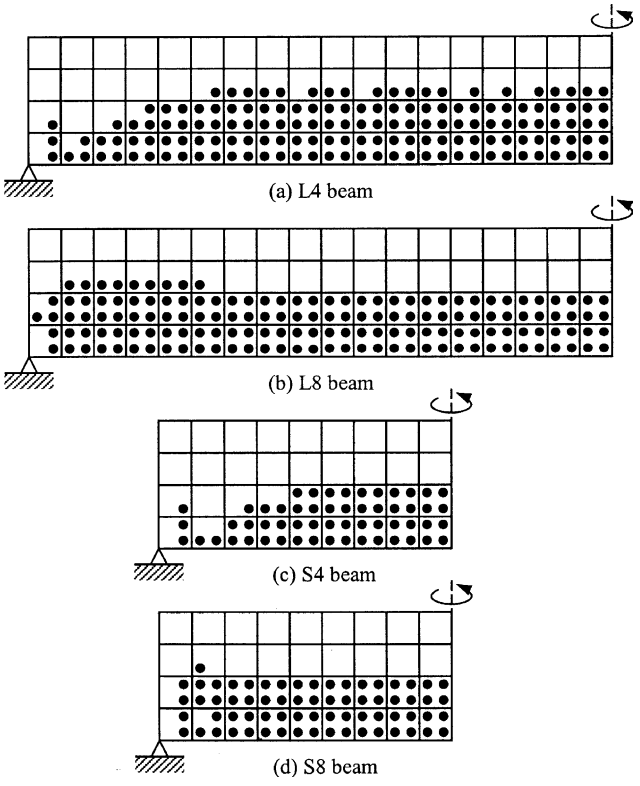

Fig. 15. Crack patterns of reinforced concrete beams strengthened by $[0]_4$ FRP at the bottom and under ultimate loads.

4.4. Ultimate analysis of reinforced concrete beams strengthened by FRP on both sides

To increase the shear resistance of the reinforced concrete beams, we consider attaching the FRP to both sides of the beams in this session. The thickness of each FRP layer is the same as before and the laminate lay-ups are $[\pm\theta]_n$, where $n = 1$, 2, 3. The fiber angle of the lamina is measured counterclockwise from the midsurface of the beams.

Figs. 16 and 17 show the typical load–deflection curves of long beams (L4 and L8) and short beams (S4 and S8) strengthened by $[\pm\theta]_3$ FRP on both sides, respectively. From these figures one can observe that when θ angle is close to 0°, the beams have the strongest stiffnesses. When θ angle is close to 90°, the beams are prone to have the weakest stiffnesses.

Figs. 18 and 19 show the increase of the ultimate load p_u versus fiber angle θ for beams with $[\pm\theta]_n$ FRP on both sides. Generally, the ultimate load p_u increases with the increasing of FRP layer numbers. For long beams with low reinforcement ratio as shown in Fig. 18(a), when $n = 1$ and 2, the increasing in p_u seems to be less independent on the fiber angle θ. However, when $n = 3$, the fiber angle does have significant influence on the ultimate load p_u and the optimal angle seems to be around

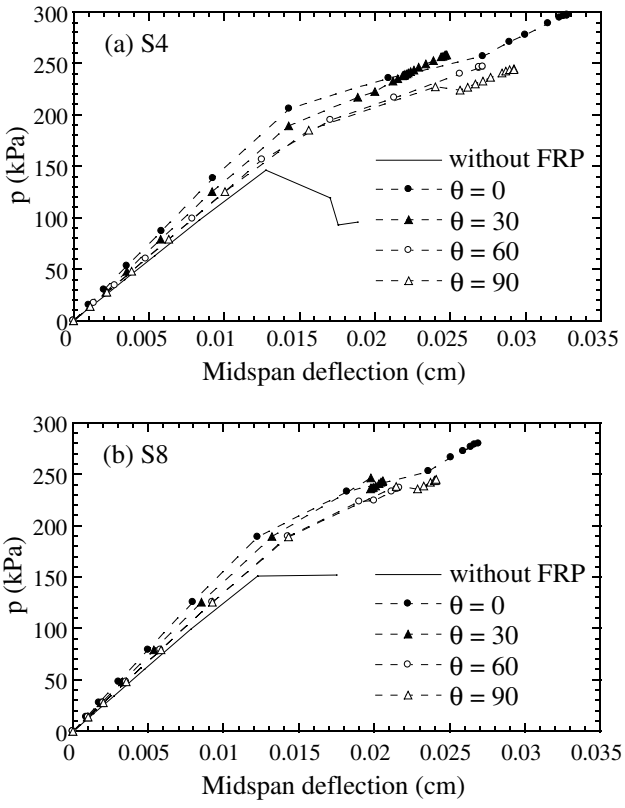

Fig. 17. Load–deflection curves of short reinforced concrete beams strengthened by $[\pm\theta]_3$ FRP on both sides.

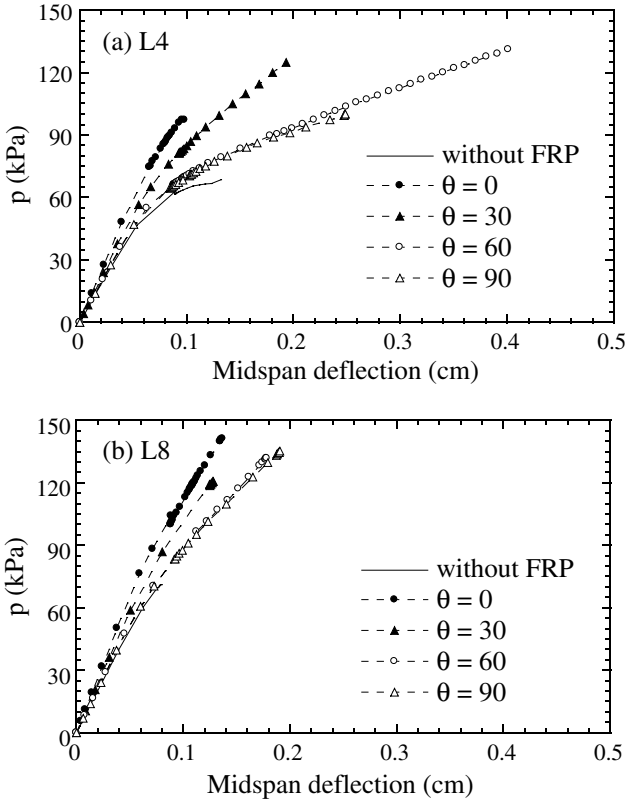

Fig. 16. Load–deflection curves of long reinforced concrete beams strengthened by $[\pm\theta]_3$ FRP on both sides.

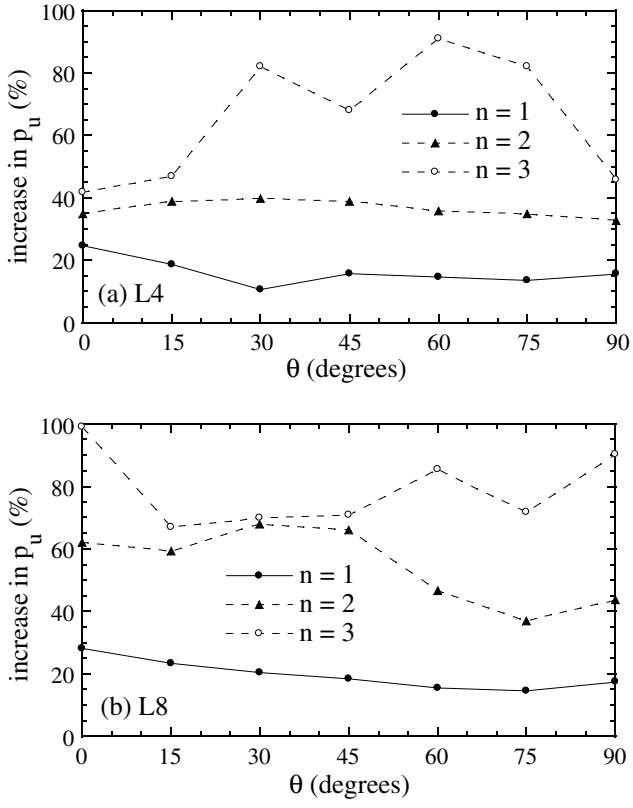

Fig. 18. Increase of p_u versus θ for long reinforced concrete beams strengthened by $[\pm\theta]_n$ FRP on both sides.

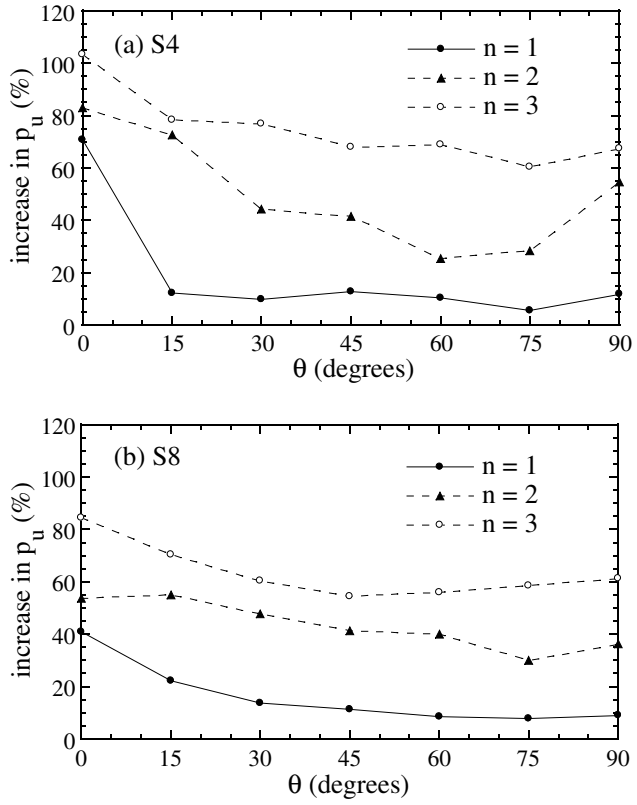

Fig. 19. Increase of p_u versus θ for short reinforced concrete beams strengthened by $[\pm\theta]_n$ FRP on both sides.

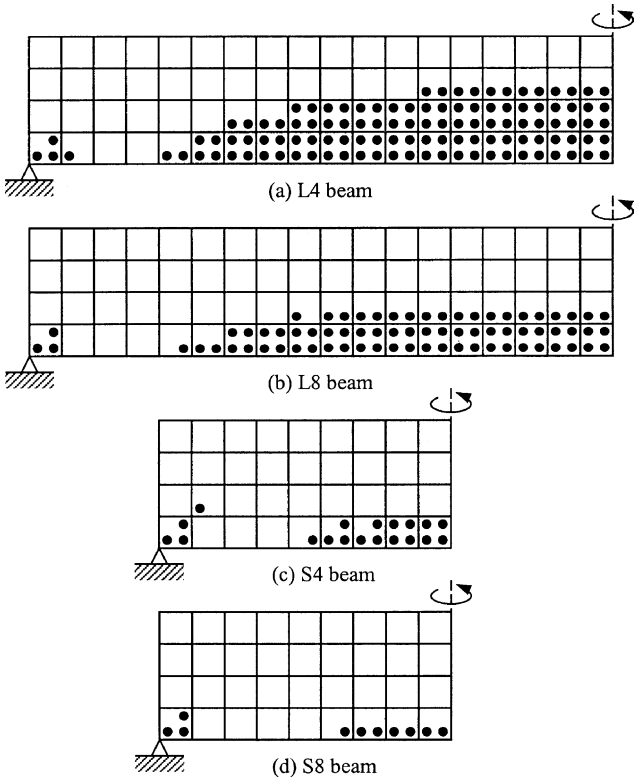

Fig. 20. Crack patterns of reinforced concrete beams strengthened by $[\pm45]_3$ FRP on both sides and under ultimate loads.

60°. For long beams with high reinforcement ratio as shown in Fig. 18(b), the increase in p_u is less dependent on the fiber angle θ only for the case with $n = 1$. For $n = 2$ and 3, the ultimate loads are highly dependent on the fiber angles. For short beams with $n = 2$ and 3 as shown in Fig. 19(a) and (b), the ultimate loads are also highly dependent on the fiber angles. For short beams with $n = 1$, the ultimate loads are less dependent on the fiber angles when the fiber angles are large, say $\theta > 15°$ for short beams with low reinforcement ratio (S4) and $\theta > 30°$ for short beams with high reinforcement ratio (S8). No matter of the reinforcement ratio and the FRP layer numbers, the optimal fiber angle of short beams seems to close to 0°.

Comparing Figs. 18 and 19 with Fig. 14, one can observe that with the same numbers of FRP layers, the ultimate strengths of beams strengthened by FRP on both sides of beams are much less than those strengthened by FRP at the bottom of beams. This indicates that to increase the bending resistance of the reinforced concrete beams is more crucial than to increase the shear resistance of the beams.

Fig. 20 shows the crack patterns of reinforced concrete beams strengthened by $[\pm45]_3$ FRP on both sides and under ultimate loads. Comparing Fig. 20 with Fig. 11, one can see that after FRP is employed on both sides of the beams, the long beams develop more cracks from central region toward the support area. For short beams, they start to develop cracks at the central-bottom region of the beams. Comparing Fig. 20 with Fig. 15, it can be seen that the beams with FRP on both sides have less cracks under the ultimate loads that those with FRP at the bottom. This is because that the ultimate strengths of the former beams are less than the latter ones.

5. Conclusions

In this paper, nonlinear finite element analyses of rectangular reinforced concrete beams strengthened by FRP are performed. Based on the numerical results, the following conclusions may be drawn:

(1) The behaviors of the beams with high reinforcement ratio and strengthened with FRP at the bottom are not influenced by the length of beam significantly.
(2) For beams with low reinforcement ratio and strengthened with FRP at the bottom, the beam lengths do affect their behaviors significantly.
(3) The beams with high reinforcement ratios and strengthened with FRP at the bottom would have more cracks at the central region than those with

low reinforcement ratios. On the other hand, the beams with low reinforcement ratios and strengthened with FRP at the bottom would have more cracks at the support area than those with high reinforcement ratios.

(4) For long beams strengthened by $[\pm\theta]_n$ FRP on both sides, when the FRP layer numbers is small, the increase in the ultimate load p_u seems to be less dependent on the fiber angle θ.

(5) For short beams strengthened by $[\pm\theta]_n$ FRP on both sides, the optimal fiber angle seems to be 0° no matter of the reinforcement ratio and the numbers of FRP layers.

(6) With the same FRP layer numbers, the ultimate strengths and the numbers of cracks of beams strengthened by FRP on both sides are much less than those strengthened by FRP at the bottom. Thus, to increase the bending resistance of the reinforced concrete beams is more crucial than to increase the transverse shear resistance of the beams.

Acknowledgements

This research work was financially supported by the National Science Council, Republic of China under Grant NSC 88-2211-E-006-014.

References

[1] Baker AA. Fiber composite repair of cracked metallic aircraft components—practical and basic aspects. Composite 1987;18(4):293–308.

[2] Ong CL, Chu RC, Ko TC, Shen SB. Composite patch reinforcement of cracked aircraft upper longeron: analysis and specimen simulation. Theor Appl Fract Mech 1990;14:13–26.

[3] Naboulsi S, Mall S. Modeling of a cracked metallic structure with bonded composite patch using the three layer technique. Compos Struct 1996;35:295–308.

[4] Schubbe JJ, Mall S. Investigation of a cracked thick aluminum panel repaired with a bonded composite patch. Eng Fract Mech 1999;63:305–23.

[5] Ritchie PA, Thomas DA, Lu L-W, Connelly GM. External reinforcement of concrete beams using fiber reinforced plastics. ACI Struct J 1991;88(4):490–500.

[6] Saadatmanesh H, Ehsani MR. RC beams strengthened with FRP plates II: analysis and parametric study. J Struct Eng (ASCE) 1991;117(11):3434–55.

[7] Nanni A. Flexural behavior and design of RC members using FRP reinforcement. J Struct Eng (ASCE) 1993;119(11):3344–59.

[8] Sharif A, Al-Sulaimani GJ, Basunbul IA, Baluch MH, Ghaleb BN. Strengthening of initially loaded reinforced concrete beams using FRP plates. ACI Struct J 1994;91(2):160–7.

[9] Chajes MJ, Januszka TF, Mertz DR, Thomson TA, Finch WW. Shear strengthening of reinforced concrete beams using externally applied composite fabrics. ACI Struct J 1995;92(3):295–303.

[10] Shahawy MA, Arockiasamy M, Beitelman T, Sowrirajan R. Reinforced concrete rectangular beams strengthened with CFRP laminates. Compos Part B: Eng 1996;27(3–4):225–33.

[11] Chambers RE. ASCE design standard for pultruded fiber-reinforced-plastic (FRP) structures. J Compos Construct (ASCE) 1997;1(1):26–38.

[12] Malek AM, Saadatmanesh H. Analytical study of reinforced concrete beams strengthened with web-bonded fiber reinforced plastic plates or fabrics. ACI Struct J 1998;95(3):343–52.

[13] Mukhopadhyaya P, Swamy N, Lynsdale C. Optimizing structural response of beams strengthened with GFRP plates. J Compos Construct (ASCE) 1998;2(2):87–95.

[14] Tedesco JW, Stallings JM, El-Mihilmy M. Finite element method analysis of a concrete bridge repaired with fiber reinforced plastic laminates. Comput Struct 1999;72:379–407.

[15] Vecchio FJ, Bucci F. Analysis of repaired reinforced concrete structures. J Struct Eng (ASCE) 1999;125(6):644–52.

[16] ASCE Task Committee on Concrete and Masonry Structure. State of the art report on finite element analysis of reinforced concrete, ASCE, 1982.

[17] Chen WF. Plasticity in reinforced concrete. McGraw-Hill; 1982.

[18] Meyer C, Okamura H. Finite element analysis of reinforced concrete structures. ASCE; 1985.

[19] Vecchio FJ, Collins MP. The modified compression-field theory for reinforced concrete elements subjected to shear. ACI J 1986;83:219–31.

[20] Hu H-T, Schnobrich WC. Constitutive modelling of concrete by using nonassociated plasticity. J Mater Civil Eng (ASCE) 1989;1(4):199–216.

[21] Hu H-T, Schnobrich WC. Nonlinear analysis of cracked reinforced concrete. ACI Struct J 1990;87(2):199–207.

[22] Hahn HT, Tsai SW. Nonlinear elastic behavior of unidirectional composite laminae. J Compos Mater 1973;7:102–18.

[23] Jones RM, Morgan HS. Analysis of nonlinear stress–strain behavior of fiber-reinforced composite materials. AIAA J 1977;15:1669–76.

[24] Hibbitt, Karlsson, and Sorensen, Inc. ABAQUS Theory Manual, User Manual and Example Manual, Version 5.8, Providence, RI, 2000.

[25] ACI Committee 318. Building Code Requirements for Structural Concrete and Commentary (ACI 318-99), American Concrete Institute, Detroit, MI, 1999.

[26] Kupfer H, Hilsdorf HK, Rusch H. Behavior of concrete under biaxial stresses. ACI J 1969;66:656–66.

[27] Saenz LP. Discussion of "Equation for the stress–strain curve of concrete" by Desayi P, Krishnan S. ACI J 1964;61:1229–35.

[28] Tsai SW, Wu EM. A general theory of strength for anisotropic materials. J Compos Mater 1971;5:58–80.

[29] Narayanaswami R, Adelman HM. Evaluation of the tensor polynomial and Hoffman strength theories for composite materials. J Compos Mater 1977;11:366–77.

[30] Rowlands RE. Strength (failure) theories and their experimental correlation. In: Sih GC, Skudra AM, editors. Failure mechanics of composites. The Netherlands: Elsevier Science Publishers; 1985. p. 71–125.

[31] Lin W-P, Hu H-T. Nonlinear analysis of fiber-reinforced composite laminates subjected to uniaxial tensile load. J Compos Mater 2002;36(12):1429–50.

[32] Jan Y-Y. Strengthening of rectangular reinforced concrete beams with fiber-reinforced composite laminated materials. MS thesis, Department of Civil Engineering, National Cheng Kung University, Tainan, Taiwan, ROC, 1997.